

# Influence of aging heat treatment on the microstructure and mechanical properties of Co<sub>29</sub>Cr<sub>31</sub>Cu<sub>4</sub>Mn<sub>15</sub>Ni<sub>21</sub> high-entropy alloys strengthened by nano-precipitates

Li Feng <sup>a</sup>, Gang Qin <sup>a,\*</sup>, Xu Yang <sup>a</sup>, Hao Ren <sup>a</sup>, Ruirun Chen <sup>a,b,\*\*</sup>

<sup>a</sup> National Key Laboratory for Precision Hot Processing of Metals, Harbin Institute of Technology, 150001, PR China

<sup>b</sup> School of Materials Science and Engineering, Shandong University of Science and Technology, Qingdao 266590, PR China



## ARTICLE INFO

### Keywords:

High entropy alloy  
Aging  
Nanoprecipitation  
Mechanical properties  
Processing technologies

## ABSTRACT

Nanoprecipitation strengthening represents a highly effective strategy for enhancing the mechanical properties of high-entropy alloys (HEAs). While existing research primarily concentrates on elucidating the strengthening mechanisms, comparatively limited attention has been paid to the processing technologies, which are equally vital for the industrial application of these materials. In this study, we systematically investigate the effects of aging heat treatment at various temperatures (300–800 °C) and durations (0.5–12 h) on the microstructure and mechanical properties of Co<sub>29</sub>Cr<sub>31</sub>Cu<sub>4</sub>Mn<sub>15</sub>Ni<sub>21</sub> HEA, which is reinforced by nanoprecipitates. Our findings indicate that aging the alloy at 700 °C for 4 h increases the yield strength from 323 MPa to 440 MPa compared to the as-cast alloy, representing a substantial enhancement in strength of 36 %. However, this improvement is accompanied by a slight reduction in plasticity. This enhancement is attributed to successfully forming uniformly distributed coherent nanoprecipitates within the alloy matrix. Furthermore, an evaluation of the strengthening contribution based on dislocation pinning theory suggests that nanoprecipitation is the predominant mechanism responsible for this increase in strength. These results underscore the critical role of processing parameters in optimizing the mechanical performance of HEAs, thereby facilitating their broader industrial applications.

## 1. Introduction

High-entropy alloys (HEAs) possess exceptional mechanical properties, corrosion resistance, and radiation tolerance, positioning them as a focal point of research in the field of metallic materials [1–5]. Furthermore, the inclusion of multiple principal elements significantly broadens the compositional design space of these alloys [6–10]. It is offering new avenues for the development of advanced metallic materials with enhanced properties tailored to meet the demands of various industrial applications [11–13]. This expansion in compositional diversity not only facilitates the optimization of material performance but also fosters innovation in the design of next-generation alloys.

Several classical strengthening mechanisms have been employed to enhance the properties of HEAs, including solid solution strengthening [14–17], fine grain strengthening [18,19], phase transformation-induced plasticity (TRIP) [20,21], and precipitation strengthening [22,23], etc. Among these, precipitation strengthening

has proven to be particularly effective in enhancing the mechanical performance of HEAs [24–28]. For example, Yang et al. [25] demonstrated a significant improvement in alloy strength by incorporating high-density, tough multicomponent nanoparticles into HEAs, resulting in both high strength and excellent plasticity. Similarly, Liang et al. [26] introduced a coherent nanostructure within the matrix, facilitating a modulated decomposition that achieved high strength while maintaining good ductility compared to HEAs without precipitation. Zhao et al. [27] overcame the strength-plasticity trade-off by triggering a multi-stage strain hardening mechanism through precise control of the size and volume fraction of the precipitated phases. Moreover, Zhao et al. [28] achieved remarkable tensile properties across a wide temperature range by introducing high-density, coherent nanoprecipitates into HEAs. While most previous studies have focused on the strengthening mechanisms associated with nanoprecipitation, there has been relatively little emphasis on the processing techniques involved. However, processing is crucial for the industrial application of these materials

\* Corresponding author.

\*\* Corresponding author. National Key Laboratory for Precision Hot Processing of Metals, Harbin Institute of Technology, 150001, PR China.

E-mail addresses: [249310025@qq.com](mailto:249310025@qq.com) (G. Qin), [ruirunchen@hit.edu.cn](mailto:ruirunchen@hit.edu.cn) (R. Chen).

[29–32]. Aging heat treatment has emerged as an effective method for promoting nanoprecipitation in alloys [23,33]. The aging temperature and time are critical process parameters that significantly influence the formation of nanoprecipitation. Therefore, conducting a comprehensive study of these parameters and their effects on the microstructure and mechanical properties of HEAs is of paramount importance. Such research will contribute to the development of high-performance alloy materials [34–39].

In this study, we systematically investigate the effect of aging heat treatment on the microstructure and mechanical properties of  $\text{Co}_{29}\text{Cr}_{31}\text{Cu}_4\text{Mn}_{15}\text{Ni}_{21}$  HEAs strengthened by nanoprecipitation. Aging treatments are conducted over a temperature range of 300–800 °C and for durations ranging from 0.5 to 12 h. We analyze the evolution of both microstructure and mechanical properties and evaluate the contribution of the precipitated phases to the overall strengthening mechanisms.

## 2. Materials and methods

### 2.1. Material preparation

The alloy ingots, with a nominal composition of  $\text{Co}_{29}\text{Cr}_{31}\text{Cu}_4\text{Mn}_{15}\text{Ni}_{21}$  in atomic proportion, were prepared using arc melting of high-purity metals (Co, Cr, Mn, Ni, and Cu, each with a purity greater than 99.9 wt%) in a high-purity argon atmosphere. To ensure chemical homogeneity, the ingots were inverted and remelted at least four times. Subsequent to the melting process, various aging temperatures and durations were applied to investigate their effects on the microstructure and mechanical properties of the alloys. The processing route employed for these alloys is illustrated in Fig. 1.

### 2.2. Microstructural characterization

The ingots were wire-cut into 5 mm × 10 mm specimens for microstructural observation. The microstructures were characterized using a scanning electron microscope (SEM, Merlin Compact) with a scanning voltage of 20 kV and a transmission electron microscope (TEM, FEI Talos F200x) with a scanning voltage of 200 kV. An energy-dispersive spectrometer (EDS, Q75) was employed to identify elemental distributions. To prepare the SEM specimens, the surfaces were sanded and then electro-polished using a 90 %  $\text{CH}_3\text{COOH} + 10\%$   $\text{HClO}_4$  solution at a working voltage of 27 V for 10 s. The phase composition of the samples was analyzed using X-ray diffraction (XRD, X-PERT) with  $\text{CuK}_\alpha$  radiation, scanned from 20° to 100° at a speed of 4°/min.

### 2.3. Mechanical properties tests

The ingots were wire-cut into specimens with dimensions of 16 mm in length, 2 mm in width, and 1.8 mm in thickness for tensile testing. Tensile mechanical properties were evaluated using a universal testing machine (Instron 5569) at ambient temperature, with a strain rate of 1 mm/min. To ensure the reproducibility of the results, each tensile test

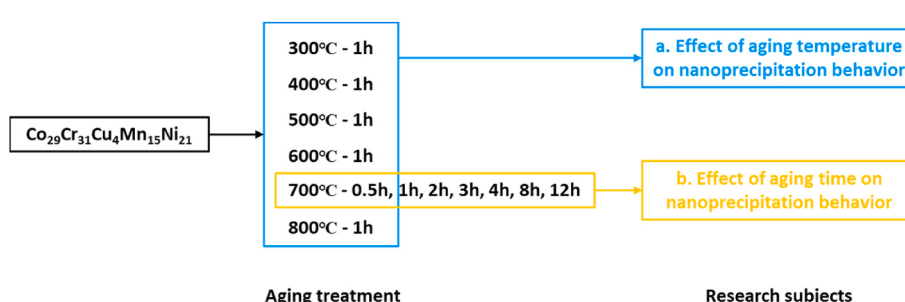
was conducted at least three times.

## 3. Results

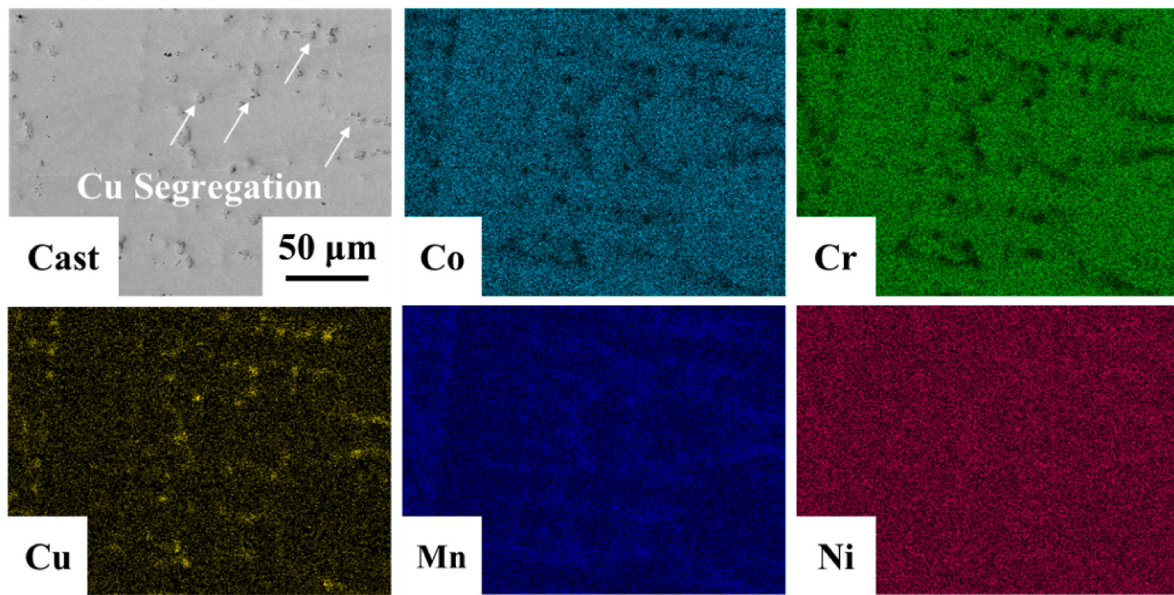
The microstructure and elemental distribution of the cast  $\text{Co}_{29}\text{Cr}_{31}\text{Cu}_4\text{Mn}_{15}\text{Ni}_{21}$  HEA are presented in Fig. 2. As depicted, the cast HEAs exhibit a characteristic dendritic crystal structure along with notable elemental segregation of copper (Cu) and manganese (Mn). As shown in Table 1, this segregation is attributed to the large positive mixing enthalpy ( $\Delta H_{mix}$ , kJ/mol) between Cu/Mn and other constituent elements (Co/Cr/Ni), which causes Cu and Mn to segregate between dendrite structures [40–42].

Fig. 3 presents the tensile engineering stress-strain curves for the  $\text{Co}_{29}\text{Cr}_{31}\text{Cu}_4\text{Mn}_{15}\text{Ni}_{21}$  HEA in both its as-cast state and after aging at temperatures ranging from 300 to 800 °C for 1 h. It was observed that after aging at various temperatures for 1 h, the yield strength of the alloys increased compared to the as-cast counterparts. Notably, the yield strength reached a peak value of 393 MPa after aging at 700 °C for 1 h, in contrast to 323 MPa for the as-cast sample, reflecting an improvement in strength of 21.6 %. Furthermore, the ultimate tensile strength of the alloy aged at 700 °C for 1 h was measured at 675 MPa, accompanied by an elongation of 56 %.

Fig. 4 displays the microstructure of the  $\text{Co}_{29}\text{Cr}_{31}\text{Cu}_4\text{Mn}_{15}\text{Ni}_{21}$  HEA after aging at temperatures ranging from 300 to 800 °C for 1 h. Consistent with the as-cast condition, Cu segregation is evident in all specimens under various aging conditions (see Figs. 2 and 4). The inset in Fig. 4 provides a local magnification at the grain boundaries. No  $\sigma$  phase precipitates are observed at the grain boundaries for aging temperatures between 300 and 500 °C. In conjunction with the engineering stress-strain curve presented in Fig. 3, it is evident that the strength of the alloy improves within the temperature range of 300–500 °C. This observation indicates that the enhancement in strength during aging at these temperatures is independent of the  $\sigma$  phase. Therefore, it can be inferred that nanoprecipitates form in the alloy during aging at 300–500 °C, and the observed increase in strength within this temperature range is attributable to the formation of these nanoprecipitates. However, at aging temperatures of 600–800 °C, a small amount of  $\sigma$  phase precipitates are detected at the grain boundaries. At 600 °C, the volume of the  $\sigma$  phase is relatively small; however, it progressively increases with rising temperature. By the time the temperature reaches 800 °C, both the volume and quantity of the  $\sigma$  phase are significantly greater than those observed at 600 °C. In conjunction with the engineering stress-strain curves presented in Fig. 3, it is evident that the strength of the alloy continues to increase when aged at 600 °C and 700 °C compared to aging at 300 °C–500 °C. Conversely, when aged at 800 °C, both the strength and plasticity of the alloy exhibit a declining trend. This phenomenon can be explained by the microstructure from 600 to 800 °C in Fig. 4, when the volume and number of  $\sigma$  phases are small, they can impede dislocation movement, thereby contributing to precipitation strengthening and enhancing the alloy's strength. However, as the volume of the  $\sigma$  phase becomes substantial, it transitions into a detrimental phase. Located at the grain boundaries, the larger  $\sigma$  phases



**Fig. 1.** Schematic representation of the various processing routes applied to the  $\text{Co}_{29}\text{Cr}_{31}\text{Cu}_4\text{Mn}_{15}\text{Ni}_{21}$  alloys.



**Fig. 2.** Microstructures and elemental distribution of the cast  $\text{Co}_{29}\text{Cr}_{31}\text{Cu}_4\text{Mn}_{15}\text{Ni}_{21}$  HEA.

**Table 1**

The enthalpy of mixing ( $\Delta H_{mix}$ , kJ/mol) between every two elements of Co, Cr, Cu, Mn, and Ni.

Element	Co	Cr	Cu	Mn	Ni
Co	–	-4	6	-5	0
Cr	-4	–	12	2	-7
Cu	6	12	–	4	4
Mn	-5	2	4	–	-8
Ni	0	-7	4	-8	–

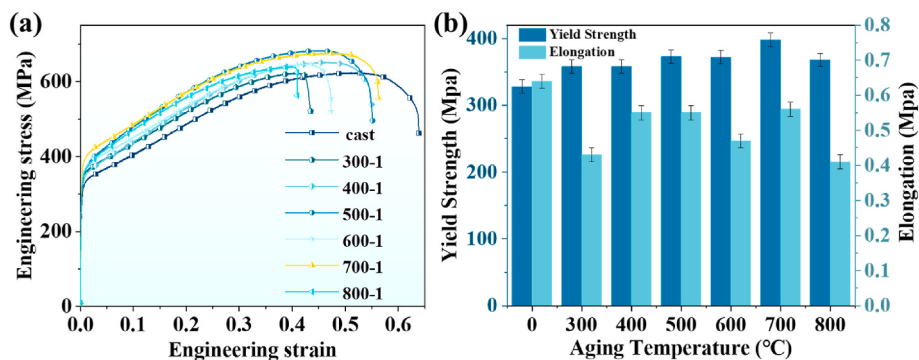
lead to stress concentration, crack initiation, and fracture propagation, ultimately resulting in premature failure of the alloy. Thus, the significant increase in  $\sigma$  phase volume at 800 °C corresponds to the observed decline in mechanical properties (see Fig. 3).

Fig. 5a presents the XRD patterns of  $\text{Co}_{29}\text{Cr}_{31}\text{Cu}_4\text{Mn}_{15}\text{Ni}_{21}$  HEA in both the as-cast state and after aging at various temperatures for 1 h. The XRD patterns reveal FCC diffraction peaks in both the as-cast condition and after aging at 300 °C, indicating a single-phase FCC structure. Fig. 5b displays the XRD pattern for the HEA aged at 800 °C for 1 h, including a magnified view of the 20 range from 39° to 49°. This pattern shows both FCC diffraction peaks and a few  $\sigma$ -phase diffraction peaks with a tetragonal structure. In contrast,  $\sigma$ -phase diffraction peaks are absent in the as-cast and 300 °C-aged samples, which is consistent with the SEM observations.

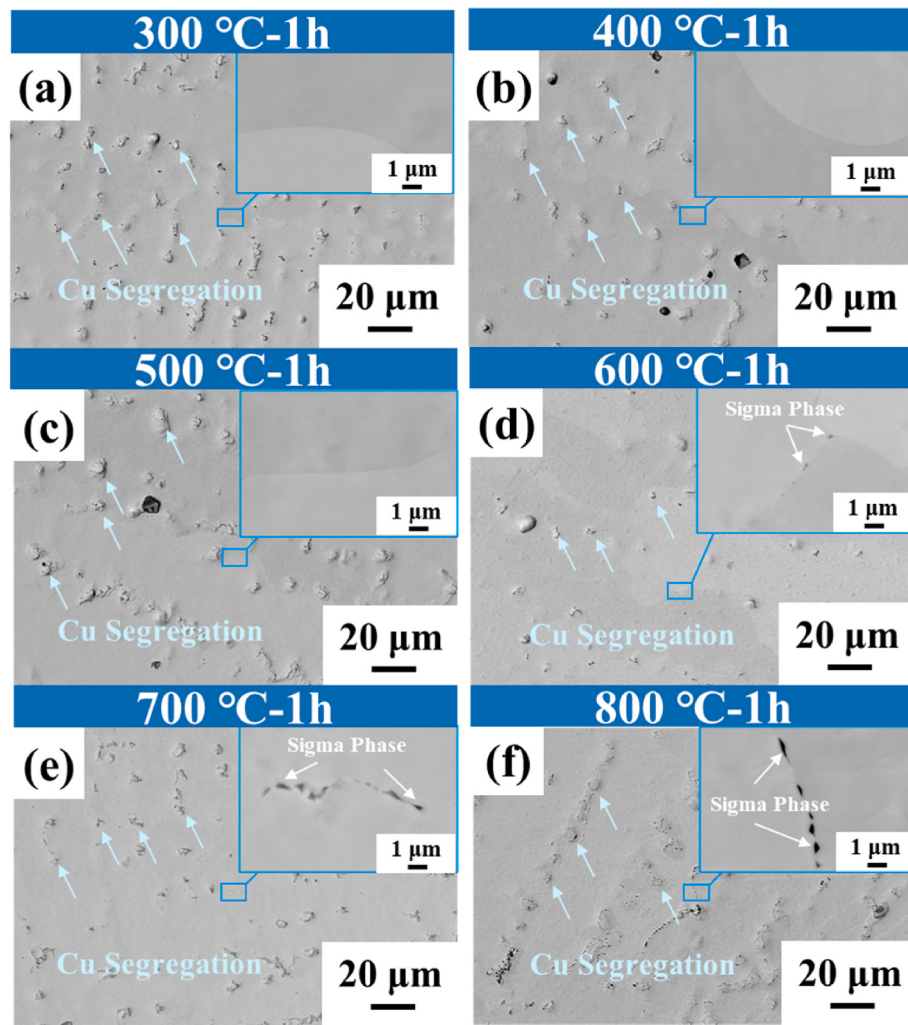
Fig. 6 presents the tensile engineering stress-strain curves for the  $\text{Co}_{29}\text{Cr}_{31}\text{Cu}_4\text{Mn}_{15}\text{Ni}_{21}$  HEA aged at 700 °C for varying durations. As illustrated in the figure, the yield strength of the alloy gradually increases with aging time from 0.5 to 4 h at 700 °C, followed by a decline after aging for more than 4 h. The ductility of the alloy decreases to varying degrees with different aging durations at 700 °C. Notably, the yield strength of the HEA reaches its maximum after aging for 4 h at 700 °C. Specifically, the yield strength of the HEA aged at 700 °C for 4 h increases from 323 MPa to 440 MPa, representing a 36 % enhancement in strength compared to the as-cast sample. Additionally, the ultimate tensile strength of the HEA aged at 700 °C for 4 h was measured at 718 MPa, with an elongation of 39 %.

Fig. 7 illustrates the microstructure of the HEA aged at 700 °C for various durations. A small quantity of the  $\sigma$ -phase is observed at the grain boundaries across all samples aged at this temperature. Combined with the analysis of the engineering stress-strain curve in Fig. 6, the plasticity of the alloy at different aging times at 700 °C is reduced to varying degrees. According to the microstructure of Fig. 7, it can be seen that this is related to the  $\sigma$  phase generated, which is not conducive to the mechanical properties of the alloy and has an adverse effect on its plasticity.

TEM tests were conducted on the HEA aged at 700 °C for 4 h to investigate the morphology of nanoprecipitates formed during aging. The TEM microstructure of the 700 °C-4 h HEA is presented in Fig. 8. Scanning Transmission Electron Microscopy (STEM) bright field image,



**Fig. 3.** Mechanical properties of the  $\text{Co}_{29}\text{Cr}_{31}\text{Cu}_4\text{Mn}_{15}\text{Ni}_{21}$  HEA in both cast and aged conditions (1 h at 300–800 °C): (a) tensile engineering stress-strain curves; (b) yield strength and elongation.



**Fig. 4.** Microstructures of the  $\text{Co}_{29}\text{Cr}_{31}\text{Cu}_4\text{Mn}_{15}\text{Ni}_{21}$  HEA aged at various temperatures for 1 h: (a) 300 °C; (b) 400 °C; (c) 500 °C; (d) 600 °C; (e) 700 °C; (f) 800 °C.

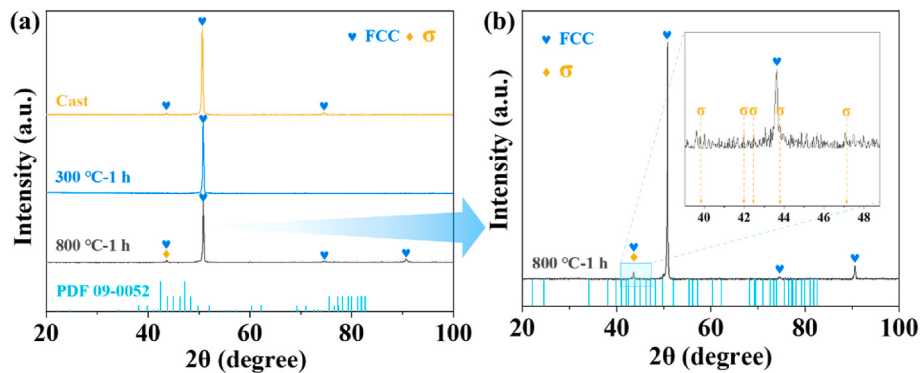


**Fig. 5.** XRD patterns of the  $\text{Co}_{29}\text{Cr}_{31}\text{Cu}_4\text{Mn}_{15}\text{Ni}_{21}$  HEA in both cast and aged conditions for 1 h at various temperatures: (a) XRD patterns of the samples in the as-cast state, aged at 300 °C for 1 h, and aged at 800 °C for 1 h; (b) XRD patterns of samples aged at 800 °C for 1 h. The presence of  $\sigma$  phase peaks and face-centered cubic (FCC) peaks is observed in the specimens.

along with the corresponding elemental distributions (Fig. 8a), reveals the generating of uniformly distributed needle-like and Cu-rich nanoprecipitates within the alloy aging heat treatment. Selected Area Electron Diffraction (SAED) pattern (Fig. 8b) obtained from the entire region depicted in the STEM image indicates a singular structural phase, suggesting that both the precipitates and the matrix share the same face-centered cubic (FCC) structure, differing only in their compositions.

Furthermore, the high-resolution TEM (HRTEM) image and the corresponding Fast Fourier Transform (FFT) image in Fig. 8c also display a single diffraction spot, confirming that the nanoprecipitates are fully coherent with the matrix. The measured crystal structure and chemical composition align well with the results obtained from XRD and SEM.

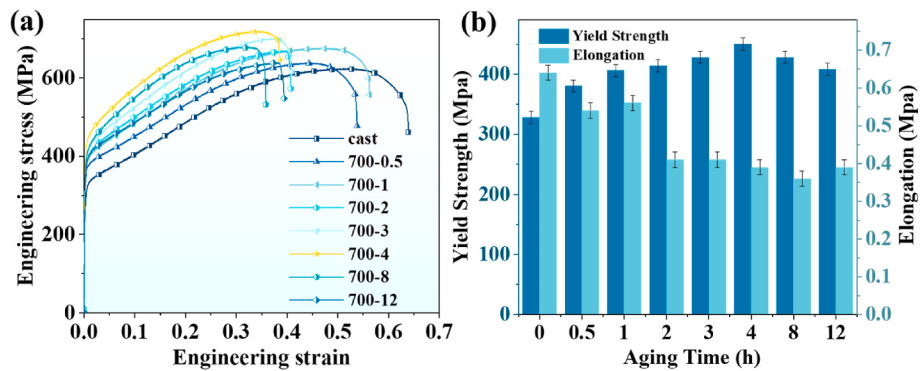


**Fig. 6.** Mechanical properties of the  $\text{Co}_{29}\text{Cr}_{31}\text{Cu}_4\text{Mn}_{15}\text{Ni}_{21}$  HEA aged at  $700\text{ }^{\circ}\text{C}$  for varying durations: (a) tensile engineering stress-strain curves; (b) yield strength and elongation.

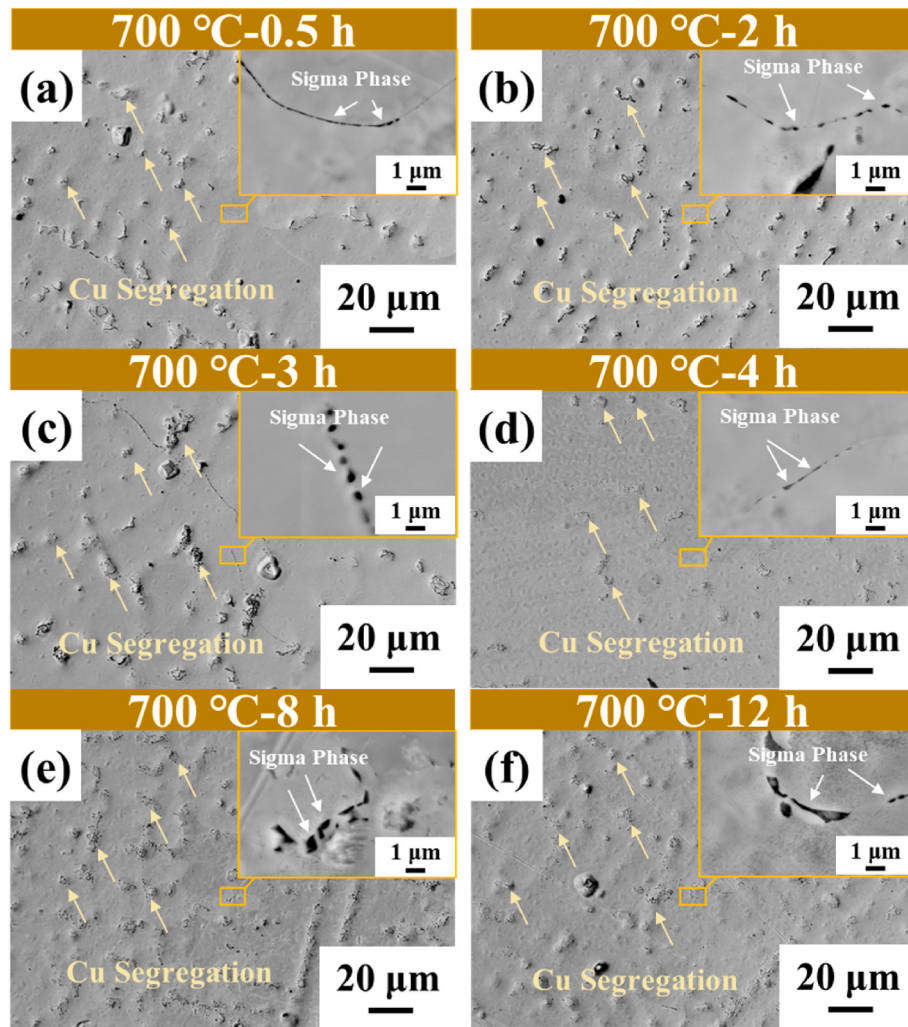


**Fig. 7.** Microstructure of the  $\text{Co}_{29}\text{Cr}_{31}\text{Cu}_4\text{Mn}_{15}\text{Ni}_{21}$  HEA aged at  $700\text{ }^{\circ}\text{C}$  for various durations: (a) 0.5 h; (b) 2 h; (c) 3 h; (d) 4 h; (e) 8 h; (f) 12 h.

#### 4. Discussions

In this study,  $\text{Co}_{29}\text{Cr}_{31}\text{Cu}_4\text{Mn}_{15}\text{Ni}_{21}$  HEA undergoes aging heat treatment under various conditions to induce nanoprecipitates that exhibit coherence with the matrix, thereby enhancing the strength of the alloy. The selection of aging parameters is crucial; excessive temperature (such as  $800\text{ }^{\circ}\text{C}$ ) or prolonged duration (such as 12 h) can lead to the precipitation of the  $\sigma$  phase at the grain boundary, which negatively

impacts the mechanical properties. The presence of larger  $\sigma$  phase particles at the grain boundaries results in stress concentration, facilitating crack initiation and propagation, ultimately leading to a reduction in the alloy's plasticity.

To elucidate the characteristics of the  $\sigma$ -phase, its morphology in the  $700\text{ }^{\circ}\text{C}-4\text{ h}$  HEA was analyzed using transmission electron microscopy, with the results presented in Fig. 9. The STEM bright-field images reveal the presence of the  $\sigma$ -phase generated in the HEA following heat

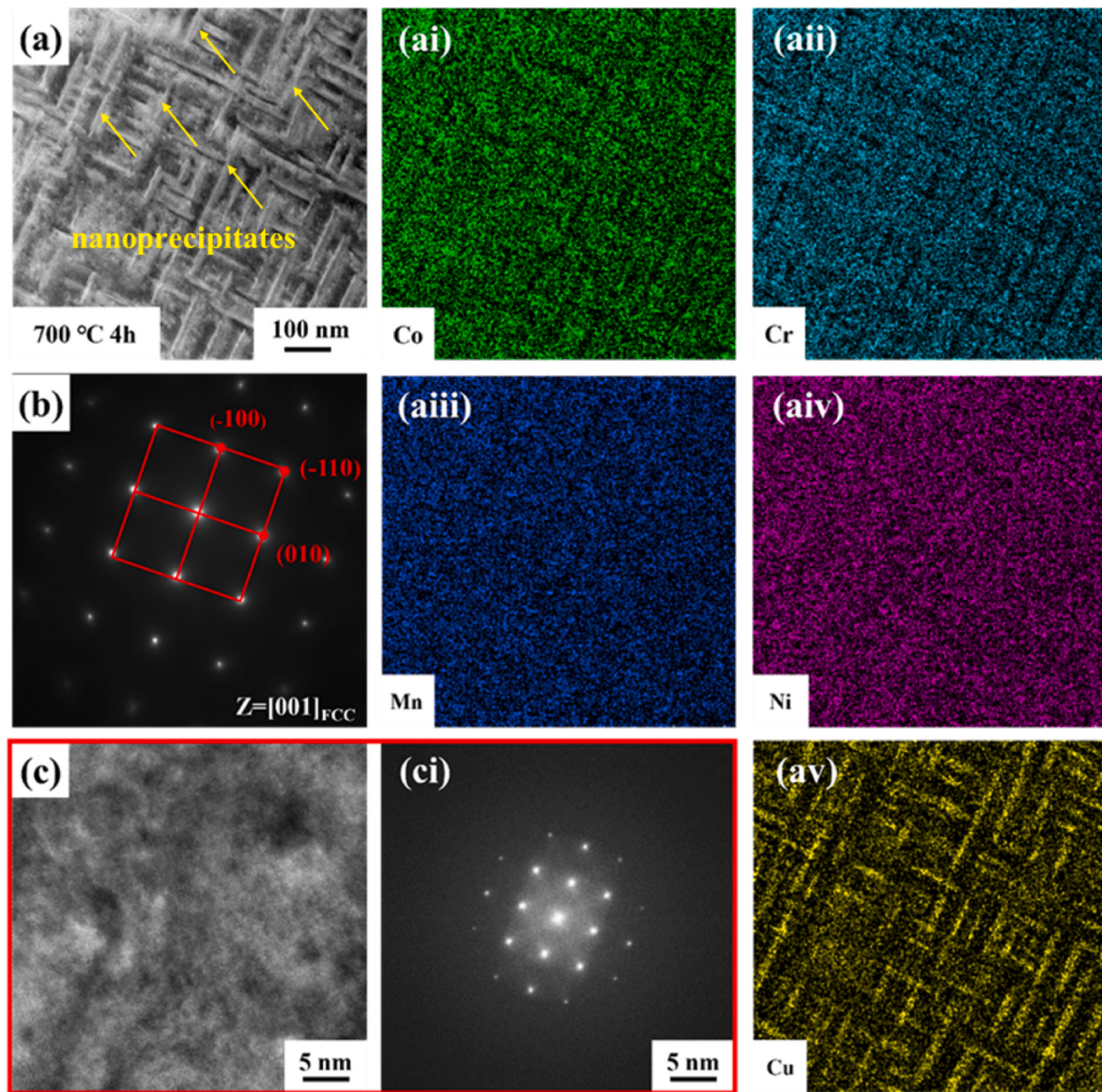


**Fig. 8.** TEM characterization of the  $\text{Co}_{29}\text{Cr}_{31}\text{Cu}_4\text{Mn}_{15}\text{Ni}_{21}$  HEA aged at  $700\text{ }^{\circ}\text{C}$  for 4 h: (a) STEM bright field image along with the corresponding elemental distribution map, illustrating the uniform distribution of high-density Cu-rich nanoparticles; (b) SAED pattern obtained from the entire area depicted in Fig. 8a; (c) HRTEM image and corresponding FFT analysis, demonstrating that the nano-precipitated phase is coherent with the matrix.

treatment at  $700\text{ }^{\circ}\text{C}$  for 4 h. The SAED pattern depicted in the illustration is derived from the  $\text{CoCr}$ -rich  $\sigma$  phase region identified in the STEM image. As illustrated, the SAED pattern along the [0, 1, 2] zone axis confirms that the crystal structure of the  $\sigma$ -phase is tetragonal. Additionally, the corresponding elemental distribution analysis demonstrates that the  $\sigma$ -phase is enriched in cobalt (Co) and chromium (Cr).

For comparative analysis, a TEM examination of the cast  $\text{Co}_{29}\text{Cr}_{31}\text{Cu}_4\text{Mn}_{15}\text{Ni}_{21}$  HEA was conducted, with the results presented in Fig. 10. STEM images and the corresponding elemental distributions reveal that the cast sample exhibits a single FCC phase devoid of nanoprecipitates. This observation underscores the effectiveness of aging heat treatment in successfully introducing uniformly distributed nanoprecipitates into the matrix, as evidenced by the results shown in Figs. 8 and 10.

Kato [43] developed a model to predict the incremental increase in critical resolved shear stress (CRSS), denoted as  $\Delta\sigma_y$ , based on Cahn's analytical framework for the strengthening of FCC alloys with spinning node structures [44]. The Kato model incorporates both lattice mismatch strengthening and modulus strengthening mechanisms [45, 46]. By considering the material to be elastically isotropic, the degree of

hardening attributable to the lattice misfit effect,  $\Delta\sigma_e$ , can be expressed as follows:

$$\Delta\sigma_e = \frac{0.5\Lambda\kappa E}{1 - \nu} \quad (1)$$

In the above expression,  $\kappa$  corresponds to the variation in lattice constant and is defined as,

$$\kappa = \frac{d(\ln a)}{dC} = \frac{\delta a}{adC} \quad (2)$$

where  $a$  is the lattice constant and  $\frac{\delta a}{dC}$  is the ratio of variation in lattice parameter between the nanoparticle and matrix over the relative change in atomic concentration. A secondary hardening contribution  $\Delta\sigma_G$  manifests from the difference in shear modulus given as,

$$\Delta\sigma_G = \frac{0.65\Delta G b}{\lambda} \quad (3)$$

where  $\Delta G$  is the difference in shear moduli of the disordered nano-

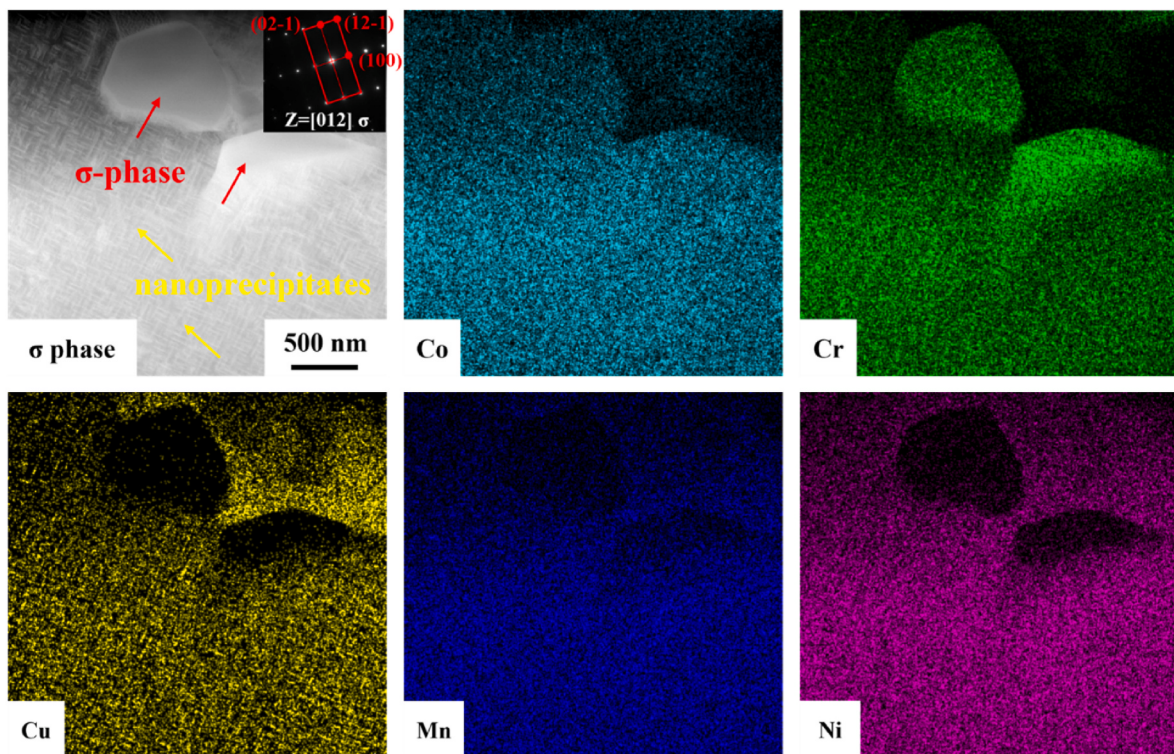


**Fig. 9.** Microstructure of the  $\text{Co}_{29}\text{Cr}_{31}\text{Cu}_4\text{Mn}_{15}\text{Ni}_{21}$  HEA after aging at  $700\text{ }^{\circ}\text{C}$  for 4 h: STEM bright field image is presented alongside the corresponding elemental distribution map. The diffraction pattern shown in the inset is derived from the CoCr-rich  $\sigma$ -phase region identified in the STEM image.

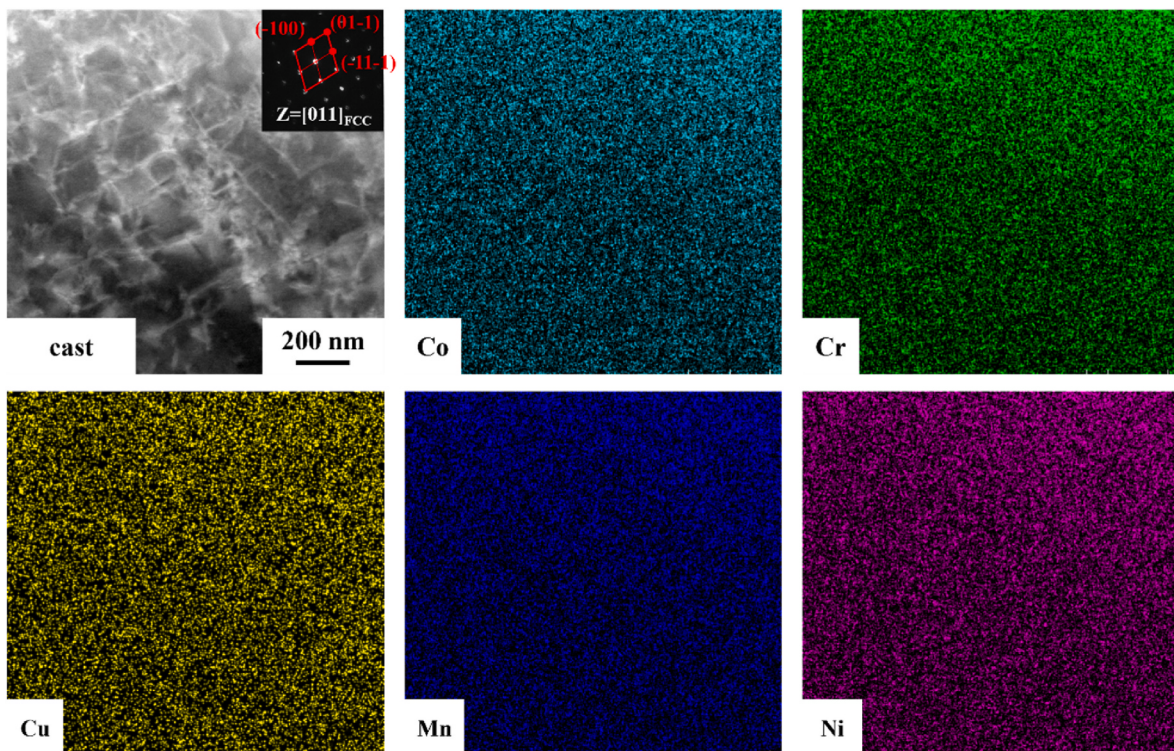


**Fig. 10.** Microstructure of the cast  $\text{Co}_{29}\text{Cr}_{31}\text{Cu}_4\text{Mn}_{15}\text{Ni}_{21}$  HEA: STEM bright field image is accompanied by the corresponding elemental distribution map. The diffraction pattern in the inset is obtained from the entire region depicted in the STEM image.

particle and matrix, and  $b$  is the dislocation burgers vector.  $\Delta\sigma_y$  is therefore expressed as,

$$\Delta\sigma_y = \Delta\sigma_e + \Delta\sigma_G \quad (4)$$

In the HEA, the precipitated phase is coherent with the matrix (see Fig. 8c); thus, the contribution to strengthening from lattice mismatch ( $\Delta\sigma_e$ ) is not considered. Instead, only the modulus strengthening contribution ( $\Delta\sigma_G$ ) is taken into account. We derived a value of  $\lambda = 20$  nm,  $G_{matrix} = 75.39$  GPa and  $G_{nanoparticle} = 108$  GPa, alongside the Burgers vector  $b = 1.443$  Å, determined through density functional theory calculations. The calculations for these parameters were conducted using the exact muffin-tin orbitals method [47], and the issue of chemical disorder in alloys was addressed within the coherent potential approximation framework [48,49]. Utilizing these parameters, we calculated that the value of  $\Delta\sigma_y$  is approximately 153 MPa, this value is in close proximity to the actual measurement of 117 MPa. This finding suggests that the increase in strength of the alloy following aging is primarily attributed to the strengthening effect of nanoprecipitation.

## 5. Conclusions

In this study, we systematically investigate the effects of aging heat treatment on the microstructure and mechanical properties of Co<sub>29</sub>Cr<sub>31</sub>Cu<sub>4</sub>Mn<sub>15</sub>Ni<sub>21</sub> nano-strengthened HEA. We employ a range of heat treatment temperatures (300–800 °C) and aging times (0.5–12 h). The principal findings are as follows.

- (1) Uniformly distributed coherent nanoprecipitates are successfully introduced into the cast Co<sub>29</sub>Cr<sub>31</sub>Cu<sub>4</sub>Mn<sub>15</sub>Ni<sub>21</sub> HEA through aging heat treatment.
- (2) The Co<sub>29</sub>Cr<sub>31</sub>Cu<sub>4</sub>Mn<sub>15</sub>Ni<sub>21</sub> HEA treated at 700 °C for 4 h exhibits a 36 % increase in strength compared to the cast alloy, with a tensile strength rising from 323 MPa to 440 MPa, albeit accompanied by a slight decline in plasticity.
- (3) When the heat treatment temperature exceeds 600 °C, Co-rich and Cr-rich σ-phases are formed at the grain boundaries.
- (4) The formation of σ-phase is detrimental to the mechanical properties of the alloys; therefore, it is critical to mitigate this phenomenon during processing.

This investigation provides valuable insights into the optimization of aging heat treatment parameters to enhance the mechanical performance of HEAs.

## CRediT authorship contribution statement

**Li Feng:** Writing – original draft, Data curation, Conceptualization. **Gang Qin:** Writing – review & editing, Methodology, Conceptualization. **Xu Yang:** Writing – review & editing, Formal analysis. **Hao Ren:** Writing – review & editing, Formal analysis. **Ruirun Chen:** Investigation, Funding acquisition.

## Declaration of competing interest

The authors declare that they have no known competing financial interests or personal relationships that could have appeared to influence the work reported in this paper.

## Acknowledgement

This work was supported by the National Natural Science Foundation of China (No. 52425401) and the Interdisciplinary Research Foundation of HIT.

## Data availability

Data not available.

## References

- [1] X. Du, S. Shuang, J. Zhao, Z. Fu, Q. Kan, X. Zhang, Extra strengthening and Bauschinger effect in gradient high-entropy alloy: a molecular dynamics study, Int. J. Mech. Sci. 264 (2024) 108829, <https://doi.org/10.1016/j.ijmecsci.2023.108829>.
- [2] Z. Gan, Y. Huang, C. Wu, T. Yang, S. Shen, G. Luo, J. Liu, Microstructural evolution and elevated-temperature strengthening mechanism of Co-free FeCrMnNi<sub>0.2</sub>Al<sub>x</sub> high-entropy alloys during annealing, Mater. Sci. Eng., A 895 (2024) 146213, <https://doi.org/10.1016/j.msea.2024.146213>.
- [3] S. Kar, V. Srivastava, G. Mandal, Low-density nano-precipitation hardened Ni-based medium entropy alloy with excellent strength-ductility synergy, J. Alloys Compd. 963 (2023) 171213, <https://doi.org/10.1016/j.jallcom.2023.171213>.
- [4] J.H. Lee, J. Lee, H. Kwon, H. Park, E.S. Kim, Y.-U. Heo, H.S. Kim, Leveraging a coarse yet strong matrix in L1<sub>2</sub>-strengthened high-entropy alloy through simplified thermomechanical processing, Mater. Sci. Eng., A 895 (2024) 146247, <https://doi.org/10.1016/j.msea.2024.146247>.
- [5] L. Wang, L. Wang, S. Zhou, Q. Xiao, Y. Xiao, X. Wang, T. Cao, Y. Ren, Y.-J. Liang, L. Wang, Precipitation and micromechanical behavior of the coherent ordered nanoprecipitation strengthened Al-Cr-Fe-Ni-V high entropy alloy, Acta Mater. 216 (2021) 117121, <https://doi.org/10.1016/j.actamat.2021.117121>.
- [6] E.P. George, D. Raabe, R.O. Ritchie, High-entropy alloys, Nat. Rev. Mater. 4 (8) (2019) 515–534, <https://doi.org/10.1038/s41578-019-0121-4>.
- [7] S.A. Sajadi, M.R. Toroghinejad, A. Rezaeian, Z. Wu, Effect of annealing treatment on microstructural and mechanical properties of a hot-forged FeCrCuMn<sub>2</sub>Ni<sub>2</sub> high-entropy alloy, Mater. 26 (2022) 101618, <https://doi.org/10.1016/j.mtla.2022.101618>.
- [8] E.P. George, W.A. Curtin, C.C. Tasan, High entropy alloys: a focused review of mechanical properties and deformation mechanisms, Acta Mater. 188 (2020) 435–474, <https://doi.org/10.1016/j.actamat.2019.12.015>.
- [9] X. Liu, S. Feng, H. Xu, C. Liu, W. Zhang, H. Zhu, W. Wei, J. Kong, Achieving exceptional strength-ductility combination in a novel L1<sub>2</sub> nanoparticles-strengthened high-entropy alloy via conventional casting, Intermetallics 165 (2024) 108160, <https://doi.org/10.1016/j.intermet.2023.108160>.
- [10] F. Haftlang, E.S. Kim, J. Kwon, Y.-U. Heo, H.S. Kim, Extraordinary combination of strength and ductility in an additively manufactured Fe-based medium entropy alloy through in situ formed η-nanoprecipitate and heterogeneous microstructure, Addit. Manuf. 63 (2023) 103421, <https://doi.org/10.1016/j.addma.2023.103421>.
- [11] G. Qin, Q. Yu, K. Yu, Y. Fang, R. Chen, Z. Liang, M. Huang, Strengthening complex concentrated alloy without ductility loss by 3D printed high-density coherent nanoparticles, Int. J. Plast. 177 (2024) 103987, <https://doi.org/10.1016/j.ijplas.2024.103987>.
- [12] H. Park, F. Haftlang, Y.U. Heo, J.B. Seol, Z. Wang, H.S. Kim, Periodic spinodal decomposition in double-strengthened medium-entropy alloy, Nat. Commun. 15 (1) (2024) 5757, <https://doi.org/10.1038/s41467-024-50078-6>.
- [13] T. Li, T. Liu, S. Zhao, Y. Chen, J. Luan, Z. Jiao, R.O. Ritchie, L. Dai, Ultra-strong tungsten refractory high-entropy alloy via stepwise controllable coherent nanoprecipitations, Nat. Commun. 14 (1) (2023) 3006, <https://doi.org/10.1038/s41467-023-38531-4>.
- [14] Y.D. Wu, Y.H. Cai, X.H. Chen, T. Wang, J.J. Si, L. Wang, Y.D. Wang, X.D. Hui, Phase composition and solid solution strengthening effect in Ti<sub>2</sub>ZrNbMoV high-entropy alloys, Mater. Des. 83 (2015) 651–660, <https://doi.org/10.1016/j.matdes.2015.06.072>.
- [15] C.-M. Lin, C.-C. Juan, C.-H. Chang, C.-W. Tsai, J.-W. Yeh, Effect of Al addition on mechanical properties and microstructure of refractory Al<sub>x</sub>HfNbTaTiZr alloys, J. Alloys Compd. 624 (2015) 100–107, <https://doi.org/10.1016/j.jallcom.2014.11.064>.
- [16] N. Park, I. Watanabe, D. Terada, Y. Yokoyama, P.K. Liaw, N. Tsuji, Recrystallization behavior of CoCrCuFeNi high-entropy alloy, Metall. Mater. Trans. A 46 (4) (2014) 1481–1487, <https://doi.org/10.1007/s11661-014-2594-5>.
- [17] J.A. Yasi, L.G. Hector, D.R. Trinkle, First-principles data for solid-solution strengthening of magnesium: from geometry and chemistry to properties, Acta Mater. 58 (17) (2010) 5704–5713, <https://doi.org/10.1016/j.actamat.2010.06.045>.
- [18] K. Cho, Y. Fujioka, T. Nagase, H.Y. Yasuda, Grain refinement of non-equiautomic Cr-rich CoCrFeMnNi high-entropy alloys through combination of cold rolling and precipitation of σ phase, Mater. Sci. Eng., A 735 (2018) 191–200, <https://doi.org/10.1016/j.msea.2018.08.038>.
- [19] B. Schuh, F. Mendez-Martin, B. Völker, E.P. George, H. Clemens, R. Pippan, A. Hohenwarter, Mechanical properties, microstructure and thermal stability of a nanocrystalline CoCrFeMnNi high-entropy alloy after severe plastic deformation, Acta Mater. 96 (2015) 258–268, <https://doi.org/10.1016/j.actamat.2015.06.025>.
- [20] M.-H. Tsai, H. Yuan, G. Cheng, W. Xu, W.W. Jian, M.-H. Chuang, C.-C. Juan, A.-C. Yeh, S.-J. Lin, Y. Zhu, Significant hardening due to the formation of a sigma phase matrix in a high entropy alloy, Intermetallics 33 (2013) 81–86, <https://doi.org/10.1016/j.intermet.2012.09.022>.
- [21] H. Huang, Y. Wu, J. He, H. Wang, X. Liu, K. An, W. Wu, Z. Lu, Phase-transformation ductilization of brittle high-entropy alloys via metastability engineering, Adv. Mater. 29 (30) (2017), <https://doi.org/10.1002/adma.201701678>.

- [22] Z. Li, K.G. Pradeep, Y. Deng, D. Raabe, C.C. Tasan, Metastable high-entropy dual-phase alloys overcome the strength-ductility trade-off, *Nature* 534 (7606) (2016) 227–230, <https://doi.org/10.1038/nature17981>.
- [23] T. Yang, Y.L. Zhao, L. Fan, J. Wei, J.H. Luan, W.H. Liu, C. Wang, Z.B. Jiao, J.J. Kai, C.T. Liu, Control of nanoscale precipitation and elimination of intermediate-temperature embrittlement in multicomponent high-entropy alloys, *Acta Mater.* 189 (2020) 47–59, <https://doi.org/10.1016/j.actamat.2020.02.059>.
- [24] Q. Wang, Z. Li, S. Pang, X. Li, C. Dong, P.K. Liaw, Coherent precipitation and strengthening in compositionally complex alloys: a review, *Entropy* 20 (11) (2018) 878, <https://doi.org/10.3390/e20110878>.
- [25] T. Yang, Y.L. Zhao, Y. Tong, Z. Jiao, J. Wei, J.X. Cai, X. Han, D. Chen, A. Hu, J. Kai, K. Lu, Y. Liu, C.T. Liu, Multicomponent intermetallic nanoparticles and superb mechanical behaviors of complex alloys, *Science* 362 (2018) 933–937, <https://doi.org/10.1126/science.aas8815>.
- [26] Y.-J. Liang, L. Wang, Y. Wen, B. Cheng, Q. Wu, T. Cao, Q. Xiao, Y. Xue, G. Sha, Y. Wang, High-content ductile coherent nanoprecipitates achieve ultrastrong high-entropy alloys, *Nat. Commun.* 9 (1) (2018) 4063, <https://doi.org/10.1038/s41467-018-06600-8>.
- [27] Y. Zhao, Y. Li, G. Yeli, J. Luan, S. Liu, W. Lin, D. Chen, X. Liu, J. Kai, C. Liu, Anomalous precipitate-size-dependent ductility in multicomponent high-entropy alloys with dense nanoscale precipitates, *Acta Mater.* 223 (2022) 117480, <https://doi.org/10.1016/j.actamat.2021.117480>.
- [28] Y.L. Zhao, T. Yang, Y.R. Li, L. Fan, B. Han, Z.B. Jiao, D. Chen, C.T. Liu, J.J. Kai, Superior high-temperature properties and deformation-induced planar faults in a novel L1<sub>2</sub>-strengthened high-entropy alloy, *Acta Mater.* 188 (2020) 517–527, <https://doi.org/10.1016/j.actamat.2020.02.028>.
- [29] L. Liu, Y. Zhang, J. Han, X. Wang, W. Jiang, C.T. Liu, Z. Zhang, P.K. Liaw, Nanoprecipitate-strengthened high-entropy alloys, *Adv. Sci.* 8 (23) (2021) 2100870, <https://doi.org/10.1002/advs.202100870>.
- [30] W. Li, D. Xie, D. Li, Y. Zhang, Y. Gao, P.K. Liaw, Mechanical behavior of high-entropy alloys, *Prog. Mater. Sci.* 118 (2021) 100777, <https://doi.org/10.1016/j.pmatsci.2021.100777>.
- [31] L. Huang, W. Lin, Y. Zhang, D. Feng, Y. Li, X. Chen, K. Niu, F. Liu, Generalized stability criterion for exploiting optimized mechanical properties by a general correlation between phase transformations and plastic deformations, *Acta Mater.* 201 (2020) 167–181, <https://doi.org/10.1016/j.actamat.2020.10.005>.
- [32] L.K. Huang, F. Liu, M.X. Huang, Accelerating bainite transformation by concurrent pearlite formation in a medium Mn steel: experiments and modelling, *J. Mater. Sci. Technol.* 176 (2024) 211–223, <https://doi.org/10.1016/j.jmst.2023.07.067>.
- [33] A. Shafiee, J. Moon, H.S. Kim, M. Jahazi, M. Nili-Ahmabadabi, Precipitation behaviour and mechanical properties of a new wrought high entropy superalloy, *Mater. Sci. Eng., A* 749 (2019) 271–280, <https://doi.org/10.1016/j.msea.2019.02.009>.
- [34] W. Deng, S. Xing, M. Chen, Effect of annealing treatments on microstructure, tensile and wear properties of cold-rolled FeCoCrNiMn high entropy alloy, *J. Mater. Res. Technol.* 27 (2023) 3849–3859, <https://doi.org/10.1016/j.jmrt.2023.10.270>.
- [35] H. Peng, S. Huang, L. Hu, I. Baker, An investigation on microstructure and mechanical properties of strong yet ductile nanoparticle-strengthened, partially recrystallized, medium-entropy alloy, *Intermetallics* 166 (2024) 108182, <https://doi.org/10.1016/j.intermet.2024.108182>.
- [36] C.N. Gonçalves, M.J. Paul, R.F. Webster, C. Kong, B. Gludovatz, G. Zepon, F. G. Coury, E.M. Mazzzer, Impact of rolling temperature on the deformation structure and mechanical performance of a CrMnFeCoNi high-entropy alloy, *J. Alloys Compd.* 971 (2024) 172585, <https://doi.org/10.1016/j.jallcom.2023.172585>.
- [37] L. Wang, Y. Xiao, Y. Ren, L. Wang, L. Wang, Y. Xue, Hierarchical nanostructure stabilizing high content coherent nanoprecipitates in Al-Cr-Fe-Ni-V high-entropy alloy, *J. Mater. Sci. Technol.* 200 (2024) 61–68, <https://doi.org/10.1016/j.jmst.2024.02.045>.
- [38] X. Zhang, B. Wan, L. Ding, C. Wang, X. Lei, Y. Weng, Z. Jia, Effect of Al and Nb addition on the precipitation hardening and deformation mechanism of CoCrNi medium entropy alloy, *J. Alloys Compd.* 992 (2024) 174619, <https://doi.org/10.1016/j.jallcom.2024.174619>.
- [39] T. Yang, Y. Zhao, J. Luan, B. Han, J. Wei, J. Kai, C. Liu, Nanoparticles-strengthened high-entropy alloys for cryogenic applications showing an exceptional strength-ductility synergy, *Scripta Mater.* 164 (2019) 30–35, <https://doi.org/10.1016/j.scriptamat.2019.01.034>.
- [40] G. Qin, R. Chen, P.K. Liaw, Y. Gao, L. Wang, Y.-Q. Su, H. Ding, J. Guo, X. Li, An as-cast high-entropy alloy with remarkable mechanical properties strengthened by nanometer precipitates, *Nanoscale* 12 (6) (2020) 3965–3976, <https://doi.org/10.1039/c9nr08338c>.
- [41] S. Ma, W. Liu, Q. Li, J. Zhang, S. Huang, Y. Xiong, B. Xu, T. Yang, S. Zhao, Mechanism of elemental segregation around extended defects in high-entropy alloys and its effect on mechanical properties, *Acta Mater.* 264 (2024) 119537, <https://doi.org/10.1016/j.actamat.2023.119537>.
- [42] D. Zhang, Y.-C. Hsu, D.C. Dunand, Ink-extrusion 3D printing and silicide coating of HfNbTaTiZr refractory high-entropy alloy for extreme temperature applications, *Adv. Sci.* (2024) 2309693, <https://doi.org/10.1002/advs.202309693>.
- [43] M. Kato, Hardening by spinodally modulated structure in b.c.c. alloys, *Acta Metall.* 29 (1981) 79–87, [https://doi.org/10.1016/0001-6160\(81\)90088-2](https://doi.org/10.1016/0001-6160(81)90088-2).
- [44] J.W. Cahn, On spinodal decomposition in cubic crystals, *Acta Metall.* 10 (3) (1962) 179–183, [https://doi.org/10.1016/0001-6160\(62\)90114-1](https://doi.org/10.1016/0001-6160(62)90114-1).
- [45] T. Xin, Y. Zhao, R. Mahjoub, J. Jiang, A. Yadav, K. Nomoto, R. Niu, S. Tang, F. Ji, Z. Quadir, D. Miskovic, J. Daniels, W. Xu, X. Liao, L.-Q. Chen, K. Hagihara, X. Li, S. Ringer, M. Ferry, Ultrahigh specific strength in a magnesium alloy strengthened by spinodal decomposition, *Sci. Adv.* 7 (23) (2021) eabf3039, <https://doi.org/10.1126/sciadv.abf3039>.
- [46] I. Basu, V. Ocelík, J.T.M. De Hosson, Size dependent plasticity and damage response in multiphase body centered cubic high entropy alloys, *Acta Mater.* 150 (2018) 104–116, <https://doi.org/10.1016/j.actamat.2018.03.015>.
- [47] Y. Li, G. Zhang, W. Wang, J. Tan, S. Zhu, On interface strengthening ability in metallic multilayers, *Scripta Mater.* 57 (2) (2007) 117–120, <https://doi.org/10.1016/j.scriptamat.2007.03.032>.
- [48] L. Vitos, H.L. Skriver, B. Johansson, J. Kollár, Application of the exact muffin-tin orbitals theory: the spherical cell approximation, *Comput. Mater. Sci.* 18 (1) (2000) 24–38, [https://doi.org/10.1016/S0927-0256\(99\)00098-1](https://doi.org/10.1016/S0927-0256(99)00098-1).
- [49] B. Gyorffy, Coherent-potential approximation for a nonoverlapping-muffin-tin-potential model of random substitutional alloys, *Phys. Rev. B* 5 (6) (1972) 2382, <https://doi.org/10.1103/PhysRevB.5.2382>.